

Topological aspects of jetting to dripping transition in step emulsifiers

Andrea Montessori,¹ Marco Lauricella,¹ Elad Stolovicki,² David Weitz,^{2,3} and Sauro Succi^{1,4,5}

¹*Istituto per le Applicazioni del Calcolo CNR, via dei Taurini 19,00185, Rome, Italy*

²*School of Engineering and Applied Sciences, Harvard University, McKay 517 Cambridge, MA 02138, USA*

³*Department of Physics, and School of Engineering and Applied Sciences, Harvard University, Pierce 231, 29 Oxford St. Cambridge, MA 02138, USA*

⁴*Center for life nanoscience at la Sapienza, Istituto Italiano di Tecnologia, viale Regina Elena 295, I/00161, Rome, Italy*

⁵*Institute for Applied Computational Science, Harvard John A. Paulson School of Engineering And Applied Sciences, Cambridge, MA 02138, United States*

(Dated: Friday 30th November, 2018)

Fully three-dimensional, time-dependent, direct simulations of the non-ideal Navier-Stokes equations for a two-component fluid, shed light into the mechanism which inhibits droplet breakup in step emulsifiers below a critical threshold of the width-to-height (w/h) ratio of the microfluidic nozzle. Below $w/h \sim 2.7$, the simulations provide evidence of a smooth topological transition of the fluid from the confined rectangular channel geometry to a isotropic (spherical) expansion of the fluid downstream the nozzle step. Above such threshold, the transition from the inner to the outer space involves a series of dynamical rearrangements which keep the free surface in mechanical balance. Such rearrangements also induce a backflow of the ambient fluid which, in turn, leads to jet pinching and ultimately to its rupture, namely droplet formation. The simulations show remarkable agreement with the experimental value of the threshold, which is found around $w/h \sim 2.4$.

PACS numbers: Valid PACS appear here

The recent surge of experimental activity in microfluidics has shown the possibility of producing controlled monodisperse oil-water emulsions, characterized by a substantial throughput of highly ordered structures often referred to as *soft flowing crystals*^{1,2,3}.

Emulsions find widespread use in many fields of science and engineering, from pharmaceuticals and cosmetics to the production of scaffolds in tissue engineering, to mention but a few^{4,5}.

In conventional microfluidic devices, such as T-junctions and flow focusers, droplets can only be produced in comparatively small amounts, hence the need to parallelize them to obtain higher throughput microfluidic systems. In these devices, the shear-induced drop pinch-off results in pressure fluctuations which determine shear force variations that inevitably lead to droplets polydispersity. On the other hand, with bulk methods⁶, based on centrifugal separation processes, throughput is significantly higher, if only at expense of a very limited control over droplet size and monodispersity.

Hence, new techniques capable of striking an optimal balance between the above conflicting requirements, are actively pursued. In this respect, step emulsification has recently captured significant interest, as a viable technique for the controlled production of liquid droplets at substantial throughput rates.^{7,8}

The main idea behind step emulsification, is to exploit the combined effect of pressure drop due to a sudden channel expansion (i.e., the step) and the elongational backflow inside the nozzle, to induce the pinch-off of the dispersed phase, thus leading to droplet formation.

A recent paper⁹, has highlighted the basic fluid phenomena underpinning the step-emulsification process, namely: (i) the backflow of the continuous phase from the exter-

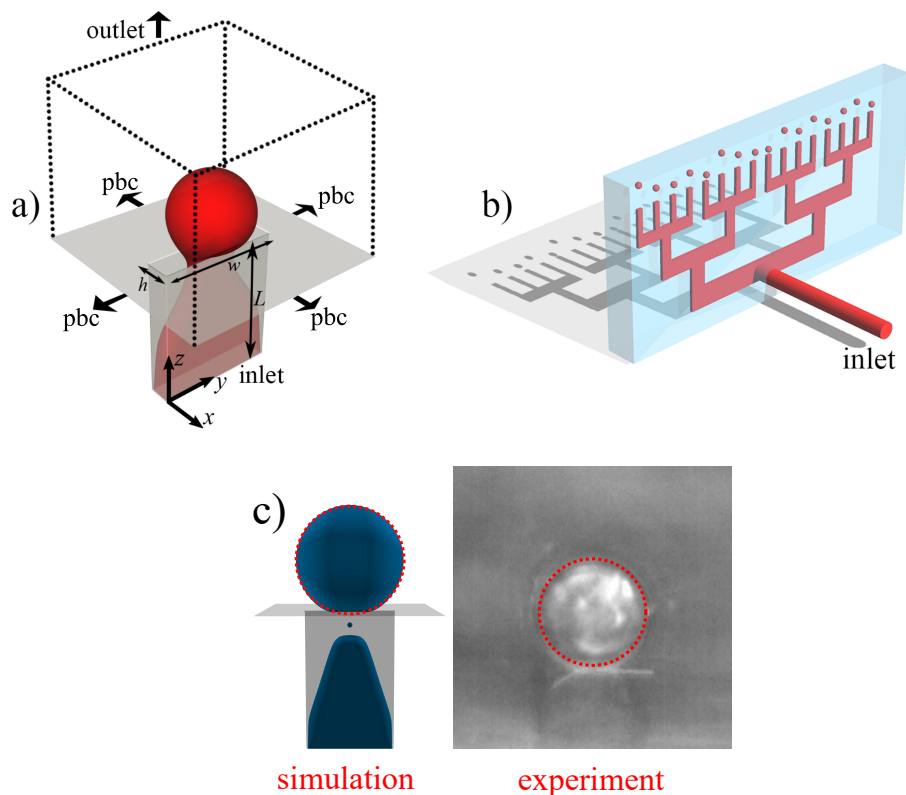


FIG. 1. Sketch of the nozzle geometry in the simulation box, along with the imposed boundary conditions [panel (a)]. The above conditions reproduce a periodic array of independent nozzles, which is consistent with the geometry of the volcano device [panel (b)]. Here, the dispersed phase (red) is pumped through the device, forming monodisperse drops in a reservoir containing a continuous immiscible phase (cyan). (c) Visual comparison between simulation and experiment of two nozzles ($h = 25\mu\text{m}$ and $w/h \sim 3$) in dripping mode. In the simulation, the very tiny droplet between the jet and the droplet is due to a secondary breakup occurring during the retraction of the jet just after the primary breakup.

nal reservoir to the confined microchannel, driven by an adverse pressure gradient, (ii) the striction of the flowing jet within the channel and its subsequent rupture, (iii) the rupture suppression upon increasing the flow speed of the dispersed phase within the channel, due to the stabilising effect of the dynamic pressure.

However, an important question is still pending: what is the mechanism which inhibits step emulsification at small values of the width-to-height (w/h) ratio?

In this short communication, we propose a potential scenario, partly based on topological considerations as suggested by extensive numerical simulations.

In particular, we performed direct numerical simulations of the fully three dimensional, time-dependent Navier-Stokes equations for a microfluidic step emulsifier geometry, using a very recent extension of the lattice Boltzmann (LB) equation for multicomponent flows, based on the color gradient method¹⁰.

In the color gradient LB for multicomponent flows, two sets of distribution functions track the evolution of the two fluid components, according the usual streaming-collision algorithm (for a comprehensive review of the lattice Boltzmann method, see^{11,12}):

$$f_i^k(\vec{x} + \vec{c}_i \Delta t, t + \Delta t) = f_i^k(\vec{x}, t) + \Omega_i^k[f_i^k(\vec{x}, t)], \quad (1)$$

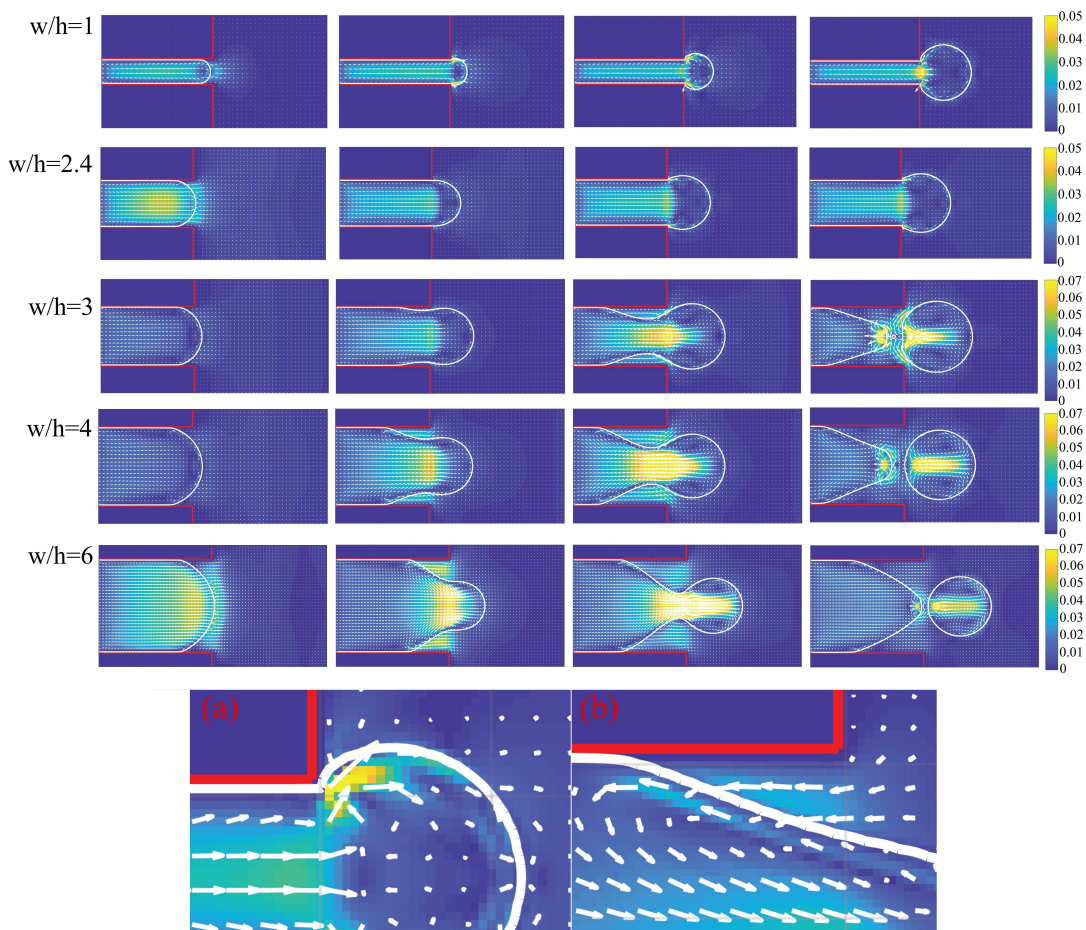


FIG. 2. Velocity field in a $y - z$ midplane taken between the two walls separated by a distance h . The first two rows show jetting nozzles. The liquid jet expands isotropically after the sudden expansion and no backflow develops within the nozzle. The other rows show breakup sequences for $w/h > 1$, from the focusing stage and pinching to the final breakup. The counterflow in the continuous phase within the nozzle is clearly evidenced by the quiver plot. The insets (a) and (b) in figure 2 show the flow field near the solid wall of the nozzle in the $x - z$ midplane for two different aspect ratios namely, 1 and 4.

where f_i^k is the discrete distribution function, representing the probability of finding a particle of the k -th component at position \vec{x} and time t with discrete velocity \vec{c}_i .

The lattice time step is taken equal to 1, and i is the index running over the lattice discrete directions $i = 1, \dots, b$, where $b = 27$ for a three dimensional 27 speed lattice (D3Q27). The density ρ^k of the k -th component and the total momentum of the mixture $\rho \vec{u} = \sum_k \rho^k \vec{u}^k$ are given by the zeroth and the first order moment of the distribution functions, respectively:

$$\rho^k(\vec{x}, t) = \sum_i f_i^k(\vec{x}, t), \quad (2)$$

$$\rho \vec{u} = \sum_i \sum_k f_i^k(\vec{x}, t) \vec{c}_i \quad (3)$$

The collision operator splits into three components^{13–15}:

$$\Omega_i^k = (\Omega_i^k)^{(3)} \left[(\Omega_i^k)^{(1)} + (\Omega_i^k)^{(2)} \right]. \quad (4)$$

In the above, $(\Omega_i^k)^{(1)}$, stands for the standard collisional relaxation¹⁶, $(\Omega_i^k)^{(2)}$ is the perturbation step¹³, which contributes to the build up of the interfacial tension. Finally, $(\Omega_i^k)^{(3)}$, is the recoloring step^{13,17}, which promotes the segregation between the two species, so as to minimise their mutual diffusion.

By performing a Chapman-Enskog expansion, it can be shown that the hydrodynamic limit of Eq.1 converges to a set of equations for the conservation of mass and linear momentum:

$$\begin{aligned} \frac{\partial \rho}{\partial t} + \nabla \cdot \rho \vec{u} &= 0 \\ \frac{\partial \rho \vec{u}}{\partial t} + \nabla \cdot \rho \vec{u} \vec{u} &= -\nabla p + \nabla \cdot [\rho \nu (\nabla \vec{u} + \nabla \vec{u}^T)] + \nabla \cdot \Sigma \end{aligned}$$

where $p = \sum_k p_k$ is the pressure and $\nu = c_s^2(\tau - 1/2)$ is the kinematic viscosity of the mixture, being τ the single relaxation time and $c_s = 1/\sqrt{3}$ the sound speed of the model^{12,16}. The stress tensor, Σ , in the momentum equation is given by:

$$\Sigma = -\tau \sum_i \sum_k (\Omega_i^k)^{(2)} \vec{c}_i \vec{c}_i \quad (5)$$

The color gradient LB scheme is further regularized by filtering out the high-order non-hydrodynamic (ghost) modes, emerging after the streaming step (see refs.¹⁸⁻²⁰ for further details).

By exploiting the regularization procedure, i.e. by suppressing the non-hydrodynamic modes, we recover the associated loss of isotropy^{10,21}.

We performed a set of simulations of the step emulsifier in the dripping regime, as it occurs for low capillary numbers. The inlet capillary number, defined as $Ca = \rho_{in} U_{in} \nu / \sigma$, (ρ_{in} is the density of the dispersed fluid, U_{in} the velocity of the dispersed phase at the inlet, ν the kinematic viscosity of the dispersed phase and σ the surface tension), was kept at a constant value ($Ca = 3 \cdot 10^{-3}$), while the w/h ratio has been varied between 1 and 6, in order to investigate its effect on the step emulsification process. The nozzle height ($h = 25 \mu m$) was discretised with 20 grid points, while the width of the channel was varied between 20 – 120 grid points corresponding to $25 \mu m$ and $150 \mu m$ retrospectively ($w/h = 1$ to $w/h = 6$). The simulations were run on a $240 \times 100 \times 120$ ($w/h = 1 - 4$) and on a $300 \times 150 \times 160$ ($w/h = 5 - 6$) nodes grid.

In this work, we simulated a single nozzle out of the full experimental device (see fig. 1 for the sketch of the nozzle and for a visual comparison between experiment and simulation), using periodic boundary conditions along cross-flow directions, in order to mimic the effect of neighbour nozzles. At the inlet and outlet, we imposed uniform velocity profiles via momentum-modified bounceback boundary conditions²². Other simulation parameters are the kinematic viscosity $\nu = 0.0333$, the surface tension of the model $\sigma = 0.1$ and the inlet velocity $U_{in} = 0.01$ (the values are reported in lattice units (all in lattice units) and chosen so to match the inlet capillary number $Ca = 3 \cdot 10^{-3}$).

The outlet velocity was chosen in order for the total mass in the system to be conserved, $U_{out} = U_{in} \cdot A_{in} / A_{out}$, where A_{in} and A_{out} are the inlet and outlet sections respectively. In figure 2, we report the time sequence of the dripping nozzles for different aspect ratios. In the dripping regime (second to fourth row in figure 2), the continuous phase flows back from the external reservoir to the confined microchannel (focusing stage) and the flowing jet ruptures as a consequence of the striction induced by such backflow. Note that the

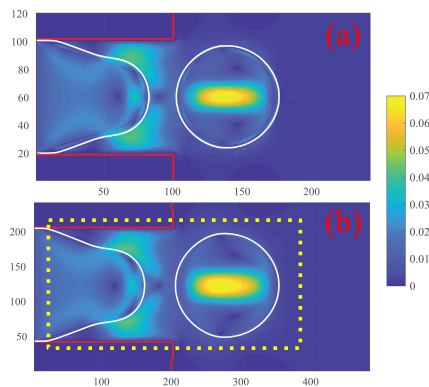


FIG. 3. Dripping nozzle simulations. Convergence test ($w/h = 4$, $y - z$ mid-plane): (a) normal resolution, (b) doubled resolution within the zone included in the rectangular area.

rupture is driven by the negative curvature, which develops in the striction region (pinching stage). In fig.2, the build-up of a significant backflow is apparent, amounting to about three times the inlet velocity. As the pinching progresses, the backflow speed decreases, due to the enlarged section available to the continuum phase. Thus, as pointed out in⁹, the breakup should not be interpreted as due to a Plateau-Rayleigh instability but rather to the backflow of the continuum phase, triggered by the adverse pressure gradient which arises in correspondence with the focusing of the water jet.

It is worth mentioning that we have tested the convergence of our simulations by carrying out a set of simulations, for $w/h = 1$ and $w/h = 4$, by doubling the resolution of the nozzle (see fig. 3). To this aim, we employed a grid-refinement procedure, as described in²³, with the additional requirement that not only the Reynolds, but also the Capillary number, are kept invariant in the transition from one grid to another. To ensure this important condition, the surface tension is scaled in such a way as to fulfill the condition:

$$Ca = \rho_{in} U_{in} \nu_R / \sigma_R = \rho_{in} U_{in} \nu / \sigma \quad (6)$$

where ν_R and σ_R are the kinematic viscosity and surface tension of the refined grid. This permits to employ a refined grid only wherever needed (i.e., around the step emulsifier nozzle), thus significantly alleviating both memory and computing time requirements.

It is now instructive to observe what happens when the width-to-height ratio of the microfluidic nozzle is being varied. The w/h ratio was varied between 1 (square section) and 6. When $w/h \leq 2.6$, the liquid jet expands isotropically after the sudden expansion and no breakup occurs. The droplet keeps expanding without breaking, in close agreement with the experiments, which predict a transition threshold around $w/h \sim 2.4$. Then, the aspect ratio has been varied between $w/h = 2.7$ and $w/h = 6$: the sequences reported in fig. 2, show the nozzles in the dripping regime. As expected, the droplet diameter is approximately constant (roughly $\sim 4h$) throughout the simulations, confirming that the droplet size is dictated by the height of the nozzle alone, regardless of the aspect ratio, this in line with other experimental evidences³.

Interestingly, we observe a saturated exponential dependence of the droplet production frequency as a function of the aspect ratio (see fig. 4). This result indicates that any further increase of the aspect ratio beyond $w/h \sim 5$ leaves the production rate basically unchanged. In a nutshell, droplet production operates in a comparatively narrow range of aspect ratios, it starts at $w/h > 2.7$ and flat-tops at about $w/h \sim 5$.

The insets (a) and (b) in figure 2 show the flow field near the solid wall of the nozzle in the $x - z$ mid-plane for two different aspect ratios namely, $w/h = 1$ and $w/h = 4$. In the former case, no re-entrant flow develops, due to the isotropic expansion of the droplet, which prevents the jet from "focusing" and the ambient fluid from entering the nozzle. As

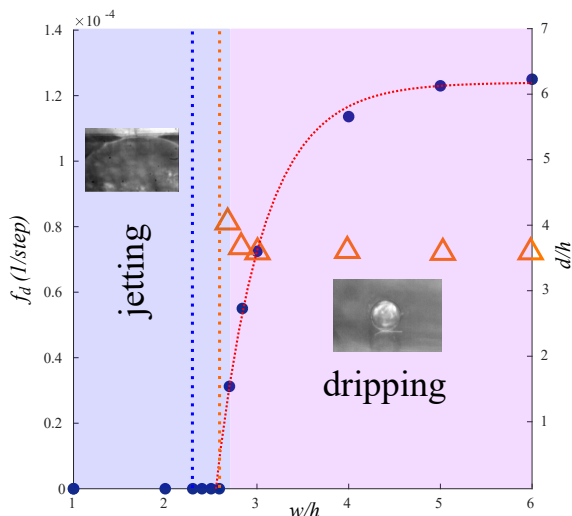


FIG. 4. Dependence of the droplet production frequency on the aspect ratio (circles). Parameters of the fitting function ($ae^{-b(w/h)} + c$): $a = -0.01832$, $b = 1.958$ and $c = 0.000124$. The non-drip to drip transition occurs above $w/h \sim 2.7$, in good agreement with experimental findings, $w/h \sim 2.4$. Triangles: d/h as a function of the width-to-height ratio. Note that the droplet diameter $d \sim 4h$, is basically independent on the aspect ratio w/h , which is in agreement with experimental findings (see^{3,9}). The vertical dotted lines (blue and orange) identify the experimental and simulation drip-to-jet thresholds, respectively.

a result, no elongational flow develops.

In the latter case ($w/h = 4$), the anisotropic expansion of the outgoing droplet leads to the necking of the liquid jet, which breaks up due to the combined effect of the Laplace pressure and the elongational backflow inside the nozzle.

A question naturally arises: what is the physical mechanism preventing the jet focusing when w/h is small?

To address this question, we shall advocate the notion of homeomorphism or topological isomorphism, namely a mapping that preserves the topological properties of a given object²⁴. Two spaces linked by a homeomorphism are called homeomorphic, indicating that, from a topological viewpoint, they are the same, because they can smoothly morphed one into another.

Despite being definitely distinct geometrical objects, a cube and a sphere are homeomorphic, while a sphere and a doughnut are not, since the latter has a hole which cannot be obtained through a smooth deformation of the sphere. In mathematical terms, the sphere has genus zero, while the doughnut has genus one. Note that curvature is by no means conserved by homeomorphisms: a sphere of radius R has curvature $1/R$, while a cube has zero curvature, since it can be opened at the edges and deposited on a plane, which is impossible with the sphere. In the step emulsifier, when $w/h \sim 1$, the fluid can continuously deform from a confined square-section shape to a spherical droplet. Topologically speaking, the two fluid objects are the same and therefore one can morph into another via an isotropic expansion, as evidenced in figure 5. On purely mathematical grounds, it would be interesting to explore whether such isotropic expansion falls within the class of Ricci flows²⁵, a subject that we leave for future investigations.

On the other hand, when w/h is greater than a critical value, around $w/h \sim 2.6$, the dynamics (i.e., the backflow driven by adverse pressure gradients) come into play and, although the parallelepiped and the sphere are still homeomorphic, the fluid undergoes a dynamic rearrangement which guarantees the curvature to be equilibrated everywhere in the system, in such way that Laplace pressure jumps remain balanced, until rupture occurs⁹. Thus,

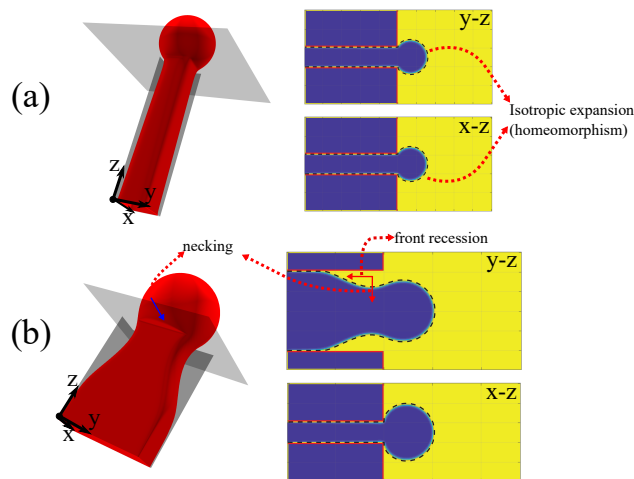


FIG. 5. (Upper panel (a)): when $w/h \sim 1$ the fluid can deform continuously from a confined square-section shape to a spherical droplet. For w/h above a critical value (larger than ~ 2.6), the fluid undergoes a dynamic rearrangement which guarantees the curvature to be equilibrated everywhere in the system, balancing the Laplace pressure jumps, until rupture occurs.

the liquid is subject to a rearrangement at the nozzle exit, as evidenced in figure 5, which shows the typical anisotropic expansion of the liquid jet in the dripping emulsifier, due to the combined effects of two different mechanisms, namely, a front recession along the flow direction and a necking of the liquid jet occurring crossflow. In this sense, surface tension is responsible for the "topological breakup" i.e., the fluid undergoes a series of (local) dynamical rearrangements in order to balance the pressure differences at the interface, which are not taken into account by a purely topological transformation.

In conclusion, fully three-dimensional, time-dependent simulations shed light on the mechanism which prevents

droplet rupture in step emulsification devices, whenever the nozzle aspect ratio is below ~ 2.7 , a value in close match with the experimental findings, yielding $w/h \sim 2.4$. When w/h is below such threshold, the liquid jet isotropically expands after the step, inhibiting the necking and preventing the ambient liquid from entering the nozzle and stretch the liquid jet until rupture. Indeed, the dispersed fluid follows a smooth transition from the confined nozzle geometry to the outer ambient, which can be interpreted as a topological isomorphism. However, whenever w/h exceeds the threshold value, a *topological breakup* is observed, i.e., although the parallelepiped and the sphere are still homeomorphic, the fluid is subject to a series of fluid-dynamical rearrangements, necessary for the curvature at any point of the free surface to keep in balance with the Laplace pressure. Eventually, these rearrangements lead to jet dripping, due to the combined effect of the backflow elongation and the Laplace gradients at the fluid interface. Despite their topological equivalence, this spontaneous symmetry breaking opens a gap between the confined parallelepiped geometry and the outer sphere, so that jet breakup is the only possibility for the former to turn into the latter.

Future work is needed to pin down the values of the breakup threshold $w/h \sim 2.7$, as well as the linear relation $d/h \sim 4$.

ACKNOWLEDGEMENT

The research leading to these results has received funding from the European Research Council under the European Union's Horizon 2020 Framework Programme (No. FP/2014-2020)/ERC Grant Agreement No. 739964 (COPMAT).

- ¹A. Montessori, M. Lauricella, and S. Succi, “Mesoscale modelling of soft flowing crystals,” *Philosophical Transaction A* 10.1098/rsta.2018.0149.
- ²P. Marmottant and J.-P. Raven, “Microfluidics with foams,” *Soft Matter* **5**, 3385–3388 (2009).
- ³E. Stolovicki, R. Ziblat, and D. A. Weitz, “Throughput enhancement of parallel step emulsifier devices by shear-free and efficient nozzle clearance,” *Lab on a Chip* **18**, 132–138 (2018).
- ⁴M. Costantini, C. Colosi, J. Jaroszewicz, A. Tosato, W. Swieszkowski, M. Dentini, P. Garstecki, and A. Barbetta, “Microfluidic foaming: A powerful tool for tailoring the morphological and permeability properties of sponge-like biopolymeric scaffolds,” *ACS applied materials & interfaces* **7**, 23660–23671 (2015).
- ⁵G. M. Whitesides, “The origins and the future of microfluidics,” *Nature* **442**, 368 (2006).
- ⁶J. O. Hinze, “Fundamentals of the hydrodynamic mechanism of splitting in dispersion processes,” *AIChE Journal* **1**, 289–295, <https://onlinelibrary.wiley.com/doi/pdf/10.1002/aic.690010303>.
- ⁷N. Mittal, C. Cohen, J. Bibette, and N. Bremond, “Dynamics of step-emulsification: From a single to a collection of emulsion droplet generators,” *Physics of Fluids* **26**, 082109 (2014).
- ⁸C. Priest, S. Herminghaus, and R. Seemann, “Generation of monodisperse gel emulsions in a microfluidic device,” *Applied physics letters* **88**, 024106 (2006).
- ⁹A. Montessori, M. Lauricella, S. Succi, E. Stolovicki, and D. Weitz, “Elucidating the mechanism of step emulsification,” *Physical Review Fluids* **3**, 072202 (2018).
- ¹⁰A. Montessori, M. Lauricella, M. La Rocca, S. Succi, E. Stolovicki, R. Ziblat, and D. Weitz, “Regularized lattice boltzmann multicomponent models for low capillary and reynolds microfluidics flows,” *Computers & Fluids* **167**, 33–39 (2018).
- ¹¹S. Succi, *The Lattice Boltzmann Equation: For Complex States of Flowing Matter* (Oxford University Press, 2018).
- ¹²T. Krüger, H. Kusumaatmaja, A. Kuzmin, O. Shardt, G. Silva, and E. M. Viggien, “The lattice boltzmann method,” *Springer International Publishing* **10**, 978–3 (2017).
- ¹³A. K. Gunstensen, D. H. Rothman, S. Zaleski, and G. Zanetti, “Lattice boltzmann model of immiscible fluids,” *Physical Review A* **43**, 4320 (1991).
- ¹⁴S. Leclaire, M. Reggio, and J.-Y. Trépanier, “Numerical evaluation of two recoloring operators for an immiscible two-phase flow lattice boltzmann model,” *Applied Mathematical Modelling* **36**, 2237–2252 (2012).
- ¹⁵S. Leclaire, A. Parmigiani, O. Malaspinas, B. Chopard, and J. Latt, “Generalized three-dimensional lattice boltzmann color-gradient method for immiscible two-phase pore-scale imbibition and drainage in porous media,” *Physical Review E* **95**, 033306 (2017).
- ¹⁶S. Succi, *The lattice Boltzmann equation: for fluid dynamics and beyond* (Oxford university press, 2001).
- ¹⁷M. Latva-Kokko and D. H. Rothman, “Diffusion properties of gradient-based lattice boltzmann models of immiscible fluids,” *Physical Review E* **71**, 056702 (2005).
- ¹⁸A. Montessori, P. Prestininzi, M. La Rocca, and S. Succi, “Lattice boltzmann approach for complex nonequilibrium flows,” *Physical Review E* **92**, 043308 (2015).
- ¹⁹R. Zhang, X. Shan, and H. Chen, “Efficient kinetic method for fluid simulation beyond the navier-stokes equation,” *Physical Review E* **74**, 046703 (2006).
- ²⁰J. Latt and B. Chopard, “Lattice boltzmann method with regularized pre-collision distribution functions,” *Mathematics and Computers in Simulation* **72**, 165–168 (2006).
- ²¹R. Benzi, S. Succi, and M. Vergassola, “The lattice boltzmann equation: theory and applications,” *Physics Reports* **222**, 145 – 197 (1992).
- ²²M. Bouzidi, M. Firdaouss, and P. Lallemand, “Momentum transfer of a boltzmann-lattice fluid with boundaries,” *Physics of fluids* **13**, 3452–3459 (2001).
- ²³A. Dupuis and B. Chopard, “Theory and applications of an alternative lattice boltzmann grid refinement algorithm,” *Physical Review E* **67**, 066707 (2003).
- ²⁴S. Lefschetz, *Introduction to topology* (Princeton University Press, 2015).
- ²⁵S. Brendle, *Ricci flow and the sphere theorem*, Vol. 111 (American Mathematical Soc., 2010).